

Processing-Microstructure Relationships in Friction Stir Welding of MA956 Oxide Dispersion Strengthened Steel

BRADFORD W. BAKER, E. SARATH K. MENON, TERRY R. MCNELLEY,
LUKE N. BREWER, BASSEM EL-DASHER, JOSEPH C. FARMER,
SHARON G. TORRES, MURRAY W. MAHONEY, and SAMUEL SANDERSON

A comprehensive set of processing-microstructure relationships is presented for friction stir welded oxide dispersion strengthened MA956 steel. Eight rotational speed/traverse speed combinations were used to produce friction stir welds on MA956 plates using a polycrystalline cubic boron nitride tool. Weld conditions with high thermal input produced defect-free, full-penetration welds. Electron backscatter diffraction results showed a significant increase in grain size, a persistent body centered cubic torsional texture in the stir zone, and a sharp transition in grain size across the thermo-mechanically affected zone sensitive to weld parameters. Micro-indentation showed an asymmetric reduction in hardness across a transverse section of the weld. This gradient in hardness was greatly increased with higher heat inputs. The decrease in hardness after welding correlates directly with the increase in grain size and may be explained with a Hall-Petch type relationship.

DOI: 10.1007/s40553-014-0033-6

© ASM International (ASM) and The Minerals, Metals, & Materials Society (TMS) 2014

I. INTRODUCTION

BECAUSE of their high-temperature strength, radiation damage resistance, creep resistance, and corrosion resistance, oxide dispersion strengthened (ODS), ferritic-martensitic (FM) steels are attractive candidates for use in a wide variety of high-temperature power production applications including fusion reactors,^[1] advanced fission and fast breeder reactors,^[2] space energy applications,^[3] and conventional power plant designs.^[4] The dispersed oxides give these materials exceptional high-temperature strength and creep resistance due to the pinning of grain boundaries and dislocations while also providing sites for the accumulation of hydrogen and helium atoms to mitigate radiation-induced swelling in nuclear applications. Although the thermo-mechanical and radiation resistance properties of ODS steels are promising, traditional fusion joining processes for these alloys, such as gas tungsten arc (GTA) and gas metal arc (GMA) welding, are unsuitable due to agglomeration of the oxide particles when the base metal melts and re-solidifies.^[5]

Agglomeration of the base metal creates a non-homogeneous distribution of oxide particles, thereby significantly reducing strength in depleted areas.

A wide array of alternative joining techniques for ODS steels has been researched including electron beam welding (EBW),^[6] laser beam welding (LBW),^[7] transient liquid phase (TLP) bonding,^[8] electro-spark deposition (ESD) welding,^[9] solid-state diffusion bonding,^[10] friction welding,^[11] and friction stir welding (FSW)^[12] with varying degrees of success and practicality. Using EBW on an ODS variant of EUROFER, Lindau concluded that EBW lead to weak weld seams.^[6] Deterioration of mechanical properties was related to the evolved microstructure in the weld zone; thus, EBW was not suitable as a joining technique for ODS alloys for highly loaded applications. Similarly for LBW, the high temperatures of LBW caused clustering of the oxide particles of PM1000 leading to a reduction of strength in the weld.^[7] To prevent agglomeration of oxide particles, alternate joining techniques that do not produce melting, such as TLP and friction welding, were studied by Krishnardula and Ambroziak, respectively.^[8,13] Although TLP bonding has been demonstrated on ODS steels such as MA956 and PM2000, the boron vapor interlayer required as a deposit between the joined materials may not be practical in all applications. This includes joining of piping systems required in the majority of cases previously mentioned. Although conventional friction welding has little effect on the oxide particle distribution, the outward flow of material during the upset of weld metal produces transverse grain boundaries in the part. This grain boundary reorientation reduces the creep resistance of the joints to that of traditional fusion welded assemblies.^[5,11,13] Using ESD to join the nanostructured ODS ferritic

BRADFORD W. BAKER, formerly Graduate Student with the Naval Postgraduate School, Monterey, CA, is now Assistant Professor with the United States Naval Academy, Annapolis, MD. E. SARATH K. MENON, Research Professor, TERRY R. MCNELLEY, Professor Emeritus, and LUKE N. BREWER, Associate Professor, are with the Naval Postgraduate School. Contact e-mail: Inbrewer@nps.edu BASSEM EL-DASHER, formerly at Lawrence Livermore National Laboratory, Livermore, CA, is now Staff Member with the Terra Power, Bellevue, WA. JOSEPH C. FARMER and SHARON G. TORRES, are with the Lawrence Livermore National Laboratory. MURRAY W. MAHONEY, Consultant, is in Provo, UT. SAMUEL SANDERSON, is with MegaStir Technologies, Provo, UT.

Manuscript submitted May 7, 2014.

Article published online October 21, 2014

alloy MA957, significant porosity was evident in the weld and degradation of the dispersed particles ultimately lead to a significant reduction of mechanical properties of the joined material.^[9] In another attempt to prevent melting of the substrates in ODS materials, diffusion bonding was used to join MA956 and PM2000, producing a bond strength 70 pct of the base materials.^[10] Unfortunately, diffusion bonding may not be practical for all applications including pipe welding. Therefore, to preserve the high-temperature strength, creep resistance, and homogenous material properties of ODS steels, FSW, a solid-state joining method, is the most promising candidate for joining these alloys for fusion or advanced energy production designs.

A number of investigations have now demonstrated that ODS steels can be joined using FSW.^[14–23] In an early investigation of FSW on MA957, Jashti *et al.* showed that this alloy could be friction stir welded, albeit with a post-weld decrease in hardness and potentially an increase in grain size in the weld nugget.^[24] Since that time, research on FSW of ODS steels has produced some common conclusions: (1) fully consolidated defect-free welds can be achieved in ODS steels using FSW, (2) FSW has a minimal impact on the oxide dispersion in the stir zone (SZ), (3) the SZ consists of coarsened and equiaxed grains, and (4) hardness in the SZ is reduced compared to the base metal (BM). Based on the current literature, increasing the heat input during FSW of fine grain MA956 is expected to increase the grain size in the SZ while consequently lowering hardness.^[15,18,19,25] While much has been learned about the microstructures and mechanical properties that result from FSW of ODS steels, these studies have each used one or two FSW conditions applied to a variety of ODS alloys, plate geometries, and tool geometries. As such, it is difficult to draw strong conclusions about the effects of FSW conditions on ODS steel microstructure and mechanical properties. In addition, these studies have focused primarily on high heat input FSW parameters (as defined by high rotational speeds and/or low traverse speeds), with the notable exceptions of Etienne's^[17] and Han's^[20] work on FSW of nanostructured

ODS steels which used low rotation speeds and high translational speeds. From a manufacturing perspective, FSW with low tool rotational speeds would reduce power requirements of the joining process and may extend tool life. Increased tool traverse speeds would decrease the welding time for a given application. The aim of the current research is to explore a broader range of FSW parameters for a single ODS steel (MA956), using a single plate and tool geometry, and to correlate this range of welding parameters with changes in microstructure and hardness.

II. EXPERIMENTAL PROCEDURE

The material used in this study was MA956 steel plate, a high-Cr, ferritic ODS steel with the material composition shown in Table I established using inductively coupled plasma mass spectrometry and LECO analysis. MA956 powder was canned and extruded at 1373 K (1100 °C, 2025 °F) and subsequently hot-rolled in three passes at 1373 K (1100 °C, 2025 °F) over 4 hours with reheating to 1373 K (1100 °C, 2025 °F) for 30 minutes before and after each rolling pass for final machining into 4 mm (0.157 in.) thick plate.

FSW of MA956 plate was accomplished by MegaStir Technologies using a tool fabricated from an MS 80 grade of PCBN and a convex scroll shoulder step spiral (CS4) tool design (25.4 mm shoulder diameter, 1.72 mm pin length, and 6 mm pin diameter), which requires no tool tilt. This same tool was used for all of the FSW passes in this paper. FSW parameters of tool rotational rate in revolutions per minute (RPM) and tool traverse speed in millimeters per minute (MMPM) were varied to produce welds of differing quality and consolidation (Table II). Plunge force was maintained constant at 17.8 kN (4000 lbf). The work piece was oriented such that the tool rotated in the $r-\Theta$ plane and traversed in the r direction with the z -axis outward normal to the plate (Figure 1). The traverse direction was parallel to the rolling direction of the plate. No observable tool wear was noted during any of the weld runs of this

Table I. The Measured Chemical Composition of MA956 (Weight Percent)

C	Cr	Al	Ti	Y ₂ O ₃	Mo	Mn	Ni	S	Si	P	Fe
0.023	19.93	4.75	0.39	0.51	0.02	0.09	0.04	0.008	0.08	0.006	bal.

Table II. Friction Stir Welding Parameter Summary

Tool Rotation Rate (RPM)	Tool Traverse Speed (MMPM)	HI	Weld Quality	Weld Penetration
200	50	4	lack of consolidation	incomplete
300	50	6	defect-free	full
300	100	3	lack of consolidation	incomplete
300	150	2	lack of consolidation	incomplete
400	50	8	defect-free	full
400	100	4	defect-free	full
400	175	2.3	lack of consolidation	incomplete
500	25	20	defect-free	full

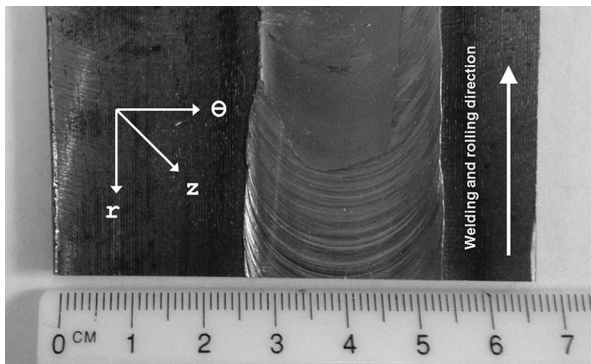


Fig. 1—Weld orientation.

research and the same tool was used for all welding; however, the total length of material welded was less than one meter. For this reason, no analysis of tool wear was attempted.

Samples of the friction stir welded MA956 plate were sectioned and analyzed by optical microscopy (OM), scanning electron microscopy (SEM), electron backscatter diffraction (EBSD), and micro-indentation. Cross-sections across the weld path were metallographically prepared for each welding condition. The cross-sections were prepared by standard metallographic preparation techniques with SiC papers, aluminum oxide polishing solutions, and 0.05 μm colloidal silica solution and then electropolished at 20 V using an electrolyte containing 10 pct perchloric acid in ethanol maintained at 250 K ($-23\text{ }^\circ\text{C}$). Microstructural examinations were conducted using a Zeiss Neon 40 field emission SEM at 20 keV. All EBSD analyses were carried out using the TSL orientation imaging microscopy (OIM) 6.0 system with a Hikari camera at 20 keV using a 60 μm objective aperture with an approximate probe current of 1 nA. EBSD data were de-noised using TSL OIM software cleanup functions of grain dilation and grain confidence index standardization in accordance with recommended settings. To ensure an adequate number of grains were counted during analyses, all inverse pole figure (IPF) maps and all pole figures were calculated from areas with minimum dimensions of $150 \times 300\ \mu\text{m}$ equating to a minimum of 2000 grains for the most limiting case. For areas of fine grain size, such as the BM, a step size of 0.25 μm was used equating to over 20,000 grains in the analysis area. For other areas with a larger average grain size, a step size of 0.5 μm was used. Microhardness measurements were performed using a HVS-1000 microhardness tester with a diamond indenter using a 1 kg-force (2.2 lbf) load and a dwell time of 15 seconds. The hardness tester calibration was verified before and after indentation using a National Institute of Standards and Technology (NIST) certified specimen with a hardness of 726 H_V and a certified error of 1.9 pct. Microhardness measurements were taken across the weld nugget at the mid-plane of the cross-section of the weld in a horizontal direction and at the retreating side (RS) thermo-mechanically affected zone (TMAZ), SZ center, and advancing side (AS) TMAZ in vertical directions.

III. RESULTS

A. Weld Consolidation

Full-penetration, defect-free welds were observed for a range of FSW conditions with higher heat input (Table II; Figures 2 and 3). Heat input is qualitatively described in this research using the ratio of the rotational speed (ω) to traverse speed (v) denoted as heat index (HI) (Eq. [1]). Weld quality and penetration were determined by macrographs of the weld nugget as a function of RPM and MPPM combinations in order to establish weld parameters to achieve defect-free microstructures. Macroscopic metallographic observations are summarized in Table II. At higher heat inputs, *i.e.*, increasing tool rotational rate and/or decreasing tool traverse speed, resulted in a defect-free nugget. Defect-free welds were observed when HI was greater than 4 (Figures 3(a) and (b)) suggesting a minimum heat input to achieve weld consolidation as shown on Figure 2. For conditions with HI less than 4, welds were observed to be defective with tunnel defects occurring at the bottom or edges of the SZ (Figures 3(c) and (d))

$$\text{HI} = \frac{\omega}{v}. \quad [1]$$

A small amount of anvil material (a mild steel) was inadvertently extracted into the bottom of some welds as shown in Figure 3(a) due to variations in thickness of the as-provided MA956 plate (note the differences in plate thickness in Figure 3). In an effort to achieve full penetration, the FSW tool penetrated through the plate thickness and contacted the support anvil. This is not uncommon, especially with variations in the plate thickness, because the tool pin tip is in very close proximity to the bottom of the plate. The material drawn into the weld nugget is not considered to be a defect associated with weld parameters but could be a defect in-service. In addition to the defects shown for the 300 RPM/100 MPPM and 300 RPM/150 MPPM conditions, similar tunnel defects were observed for RPM/MPPM combinations of 200 RPM/50 MPPM and 400 RPM/175 MPPM leading to lack of consolidation in the weld nugget.

The nugget zones formed during the welding accomplished in this research were basin-shaped as opposed to elliptical as defined by Mishra (Figure 3). Additionally, as already discussed by Mishra and several authors, the shape of the nugget zone is dependent on FSW parameters.^[26] Clearly, with greater heat input, Figures 3(a) and (b), the weld nugget is very broad both at the weld crown and weld root. In comparison, for lower heat input parameters, Figures 3(c) and (d), the width of the weld nugget is narrow at the weld root. This change in shape is best visualized by looking at the weld nugget width at the centerline of the plate.

B. Stir Zone Microstructures

Each FSW parameter combination produced a stir zone (SZ) microstructure with coarsened and nearly

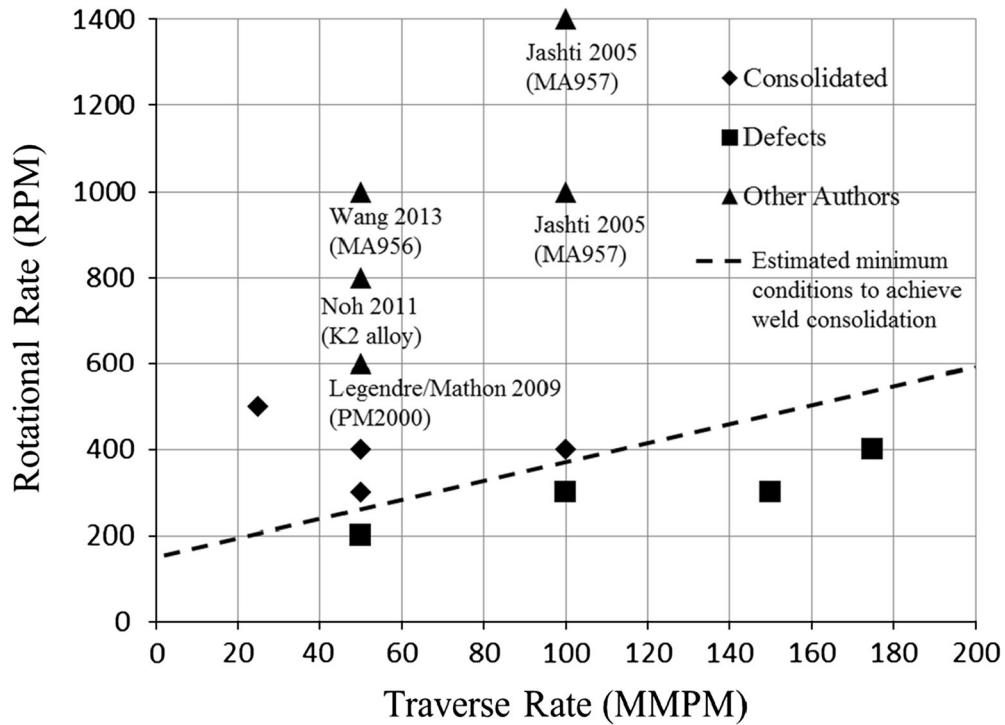


Fig. 2—Friction stir welding parameter map illustrating weld parameters for defect-free welds. The dotted line is illustrative of proposed minimum conditions to achieve weld consolidation. Triangles represent conditions used by other authors on similar alloys.

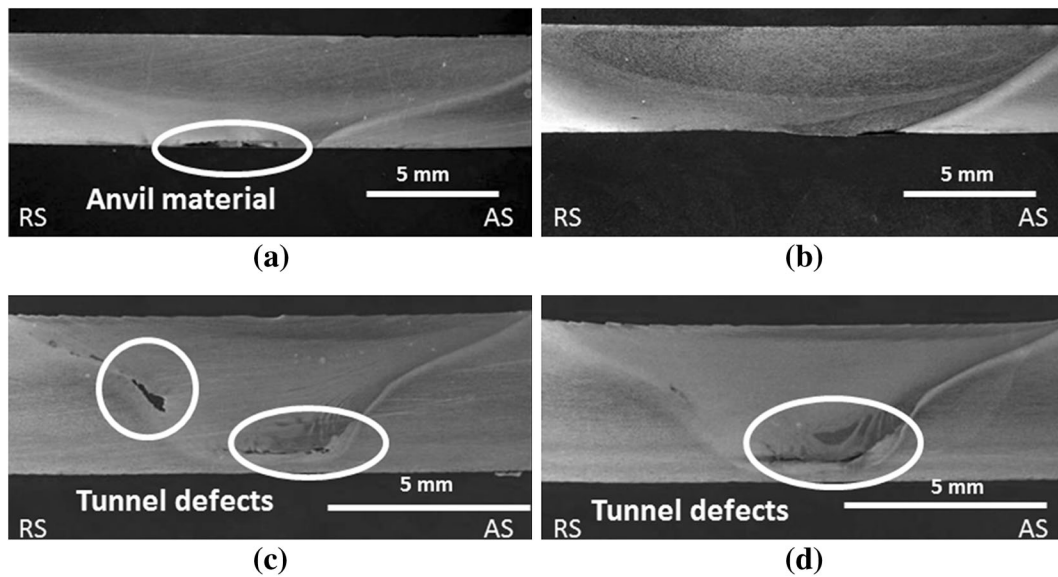


Fig. 3—Optical macrographs of transverse metallographic cross-sections for (a) 400 RPM/100 MMPM and (b) 500 RPM/25 MMPM weld parameter combinations showing full-penetration defect-free welds and (c) 300 RPM/100 MMPM and (d) 300 RPM/150 MMPM combinations showing tunnel defects nominally occurring on the retreating side and root of the weld.

equiaxed ferrite grains, a significantly lower average hardness value compared to the BM, and a BCC torsional texture. Similar to the BM, the SZ microstructure remained a single ferritic phase with no phase transformations noted in the base alloy. The microstructure in the SZ for all the different FSW parameter sets exhibited significant grain coarsening in the SZ compared to the very fine average grain size of $0.89 \mu\text{m}$

in the BM (Figure 4). For each FSW parameter combination, grain size was highest in the center of the SZ and decreased moving outward toward the BM. No abnormal grain growth was noted in any area of any sample. The grain size reduction, traversing from the SZ to the BM, was not symmetric. For example, the grain size reduction was gradually moving from the SZ toward the retreating side (RS). Similarly, a gradual

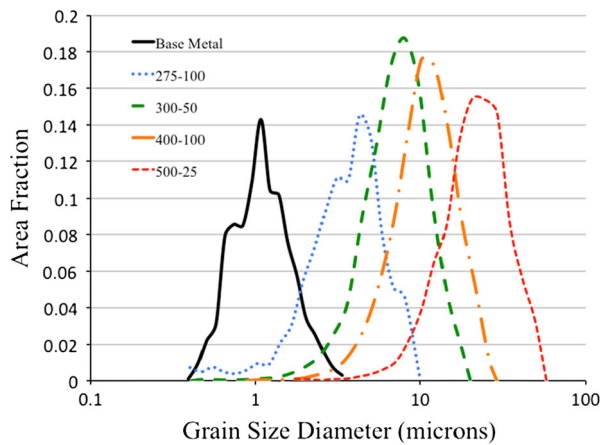


Fig. 4—SZ grain size distributions for different FSW parameters (RPM–MMPM) showing a systematic increase in grain size as a function of welding parameters.

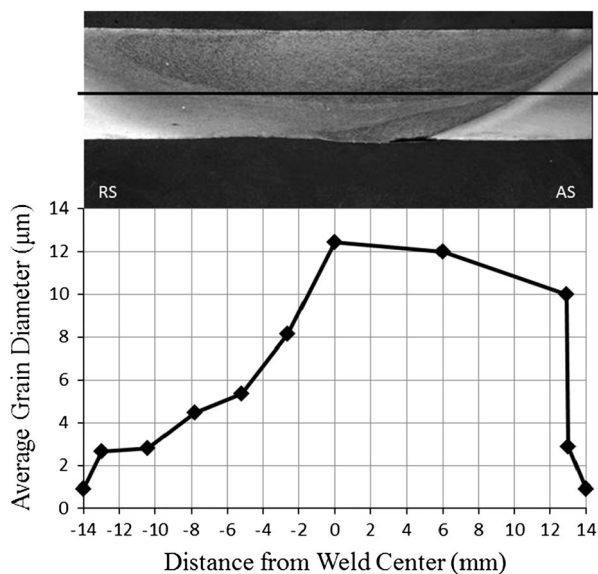


Fig. 5—Average grain diameter for 500 RPM/25 MMPM weld parameters along the mid-plane of weld.

grain size reduction was observed moving outward from the SZ toward the advancing side (AS), but a sharp gradient in grain size was present at the thermo-mechanically affected zone (TMAZ) boundary. These grain size gradients were present across all FSW weld parameter sets, although the grain size reduction gradient on the AS-TMAZ boundary was most dramatic for the 500 RPM/25 MMPM welding condition corresponding to the highest heat input used in these experiments (Figure 5).

Closer examination of the high-angle and low-angle grain boundary (HAGB and LAGB, respectively) structures show that while the grain size defined by HAGBs increased systematically with increasing heat input (black lines in Figure 6), a persistent LAGB structure was present for all microstructures. LAGBs are defined here as grain boundaries with scalar misorientations between 1 and 10 deg (bold red lines

in Figure 6). The grain boundary network for each microstructure was comprised of approximately 20 pct LAGBs (ranging from 17.0 to 23.8 pct), regardless of heat input. In the 400 RPM/100 MMPM grain boundary map (Figure 6(c)), many of the larger oxide particles were incorrectly detected as low-angle grain boundaries and thus the 400 RPM/100 MMPM condition showed an incorrectly high percentage of 38.2 pct LAGBs.

Scanning electron images from the BM (Figure 7(a)) and the SZ (Figure 7(b)) suggest two initial important details: (1) SZ grains are noticeably larger than BM grains and (2) oxide particles appear to be coarsened in the SZ. X-ray spectra collected from these coarsened particles show increased yttrium, aluminum, and oxygen signals compared with the based alloy (Figures 7(c) and (d)). A detailed characterization of the oxide dispersion is beyond the scope of this paper, but these microscale data demonstrate that FSW has caused oxide particle coarsening clearly visible at the microscale. Other research on FSW effects on oxide particle size and distribution is inconclusive. Miao and Etienne separately used transmission electron microscopy (TEM), small angle neutron scattering (SANS), and atom probe tomography (APT) on FSW samples of MA957 to determine that FSW had a small effect on the distribution of oxide particles in the weld^[9,17] while other research on FSW of other ODS alloys has shown modest coarsening of oxide particles during FSW.^[14,15,25] Chen and Tatlock have shown that the yttria in PM2000 reacts with aluminum during processing of the plate and during FSW to generate two yttrium aluminum oxides: yttrium aluminum garnet (YAG) and yttrium aluminum perovskite (YAP). A full review of the effect of FSW on oxide particles is forthcoming, but initial results suggest a growth and transformation of Y-Al-O particles due to the heat input from FSW that causes the particle coarsening evident in Figure 7. Further details concerning the characterization of oxide particles can be found in the dissertation work of Baker.^[27]

For each FSW combination, hardness decreased across the weld nugget (Table III and Figure 8). Each hardness data point in Figure 8 represents the average of three hardness measurements to account for data scatter. Experimental error associated with hardness measurements was 1.9 pct for homogeneous areas such as the BM and SZ; however, variations up to 10 pct were seen in the TMAZ with as little as 300 μm spacing between indentations. This data scatter was attributed to actual hardness variations due to the sharp spatial gradients in hardness at the SZ-TMAZ boundary rather than to experimental error. A plot of hardness variations from the top to the bottom of the friction stir weld for the 500 RPM/25 MMPM condition is shown in Figure 9. There is little change in hardness in the SZ through the depth of the weld; however, traversing across the TMAZ along a vertical line at a horizontal distance away from the center of the SZ, dramatic, and rapid changes in hardness occur. This shift in hardness would be expected as the hardness trace crosses through

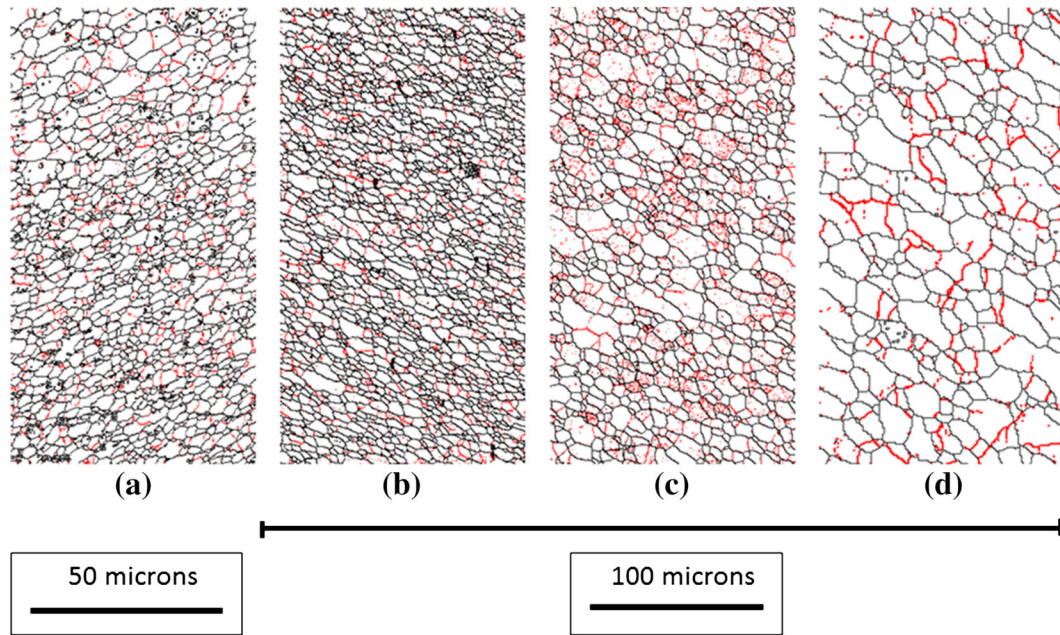


Fig. 6—SZ grain size maps for (a) 275 RPM/100 MMPM, (b) 300 RPM/50 MMPM, (c) 400 RPM/100 MMPM, and (d) 500 RPM/25 MMPM combinations. Bold/red lines indicate LAGBs ($1 < \theta < 10$ deg). Black lines indicate HAGBs ($\theta > 10$ deg) (Color figure online).

a range of microstructures, *i.e.*, weld nugget, TMAZ, heat affected zone (HAZ), and BM. This change is most abrupt on the AS TMAZ.

Pole figures from the SZ for each FSW condition displayed a persistent, torsional texture (Figures 10(b) through (e)), which is distinctly different from the rolling texture in the BM (Figure 10(a)). The BM-rolled texture contained a γ fiber with a $(1\ 1\ 1)(\bar{1}\bar{1}\ 0)$ orientation consistent with other rolled BCC materials.^[28] The degree of texture in the SZ did appear to decrease systematically as the heat input increased, as noted by the intensities in the contoured pole figures. Similar experimental results have been shown for both torsional steel textures and friction stir welded SZ textures for other ODS steels.^[19,20,28]

C. Thermo-mechanically Affected Zone

The microstructure changed abruptly at the boundary between the SZ and TMAZ. This change was most pronounced for high heat input conditions and was consistently greater on the AS versus the RS of the tool for each FSW condition. The most gradual grain size transition at the AS-TMAZ boundary occurred for the 400 RPM/100 MMPM combination, corresponding to the lowest heat input condition of the three welds studied in detail. The SZ-TMAZ interfaces for each FSW combination are shown in Figure 11 with contrastingly increasing gradients in grain size as heat input increases.

Grain size gradients were much lower on the RS for each FSW parameter combination and therefore were not visible on a single orientation (inverse pole figure or IPF) map. To compensate for this, a series of smaller IPF maps were analyzed along the RS of each weld. The results show a gradual reduction in grain size across the

RS. Figure 12 is a representative example of IPF maps across the entire weld nugget.

IV. DISCUSSION

Successful FSW was accomplished over a wide range of welding conditions. In this paper, the term HI is used for comparing these various FSW conditions, while fully acknowledging that it is not a quantitative measure of the heat input. This simple ratio of the tool rotational speed to the tool traverse speed is the inverse of weld pitch^[29,30] and has been used in previous literature as a means for predicting weld consolidation.^[31] In the present investigation, the tool, plunge force, and material for these experiments were fixed. As shown in the macrographs of Figure 3, weld defects occurred for low HI conditions. This observation is similar to work by Chimbli who systematically observed a lack of consolidation in friction stir welded aluminum alloys as the rotational speed decreased and/or the traverse speed increased.^[32] For the MA956 material in this work, a minimum HI value between 4 and 6 produced consolidated, defect-free welds. For comparison, other research on FSW of ODS steels has generally used rotational speeds larger (600 to 1000 RPM) than those reported here (200 to 500 RPM).^[14,15,18,19,24,25] In 2011, Han did report successful FSW on an experimental ODS steel with a low rotational speed of 150 RPM, with a rotational speed of 150 RPM.^[20] In addition, Etienne *et al.*, reported results on FSW of commercial MA957 with a rotation speed of 130 to 160 RPM and a traverse speed range of 150 to 200 MMPM; however, this work did not discuss the macroscopic characteristics of the weld.^[17] The FSW heat input is a complex function of tool geometry, FSW machine design, plunge force and

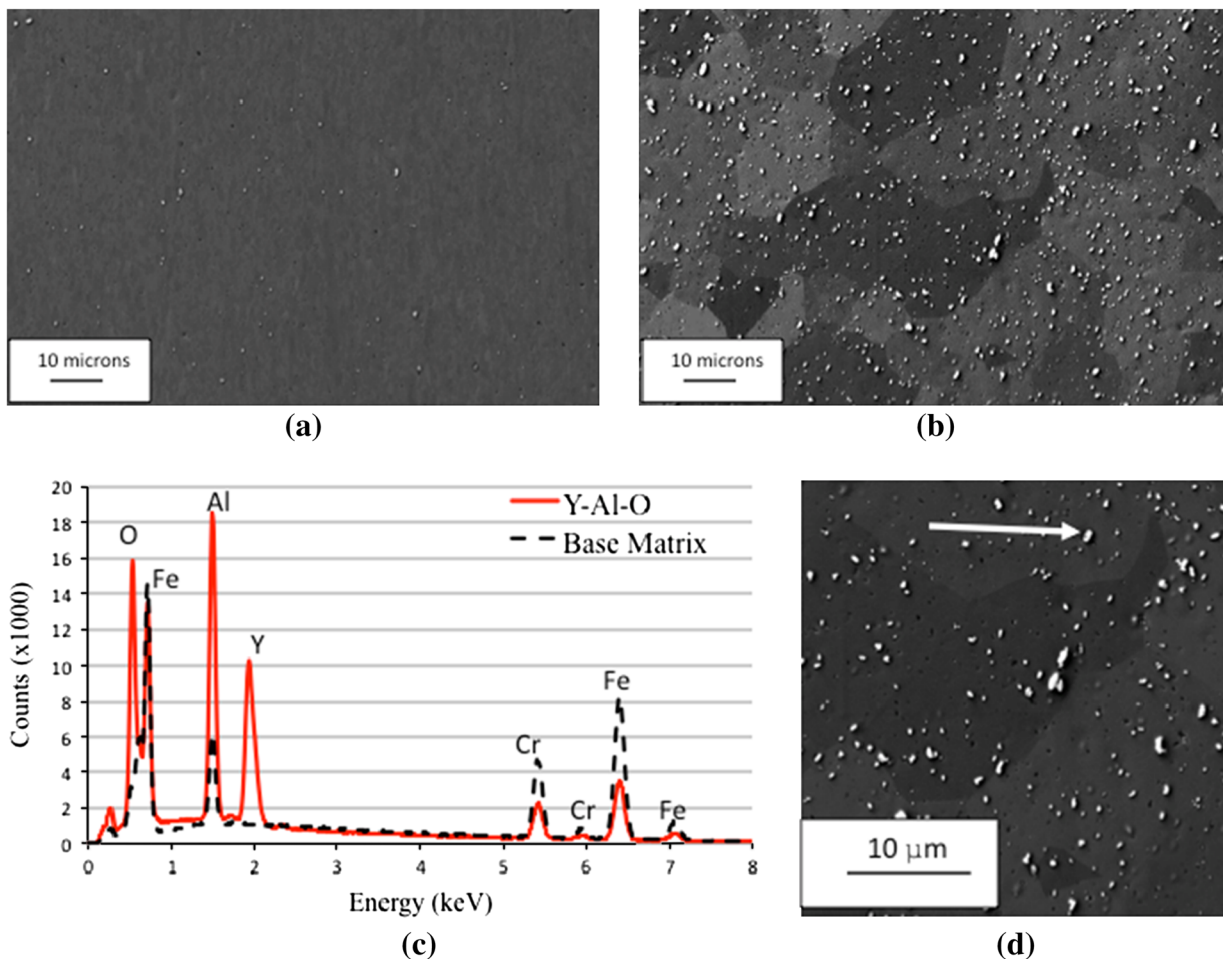


Fig. 7—SEM micrographs of (a) BM and (b) SZ with parameters of 500 RPM/25 MMPM showing qualitative oxide particle coarsening following FSW. Both images are at the same scale and dispersed oxide particles and grains are barely visible in (a) while both coarsened oxide particles and grains are clearly visible in (b) after friction stir welding. An energy dispersive X-ray spectrum (c) shows the increase in yttrium, aluminum, and oxygen signals in a single oxide particle (red spectrum) over those in the base metal (black spectrum). (d) Shows the particle from which the X-ray spectrum was collected (Color figure online).

Table III. Stir Zone Grain Size Diameter and Hardness for Friction Stir Welding Parameter Conditions

FSW Condition (RPM/MMPM)	SZ Grain Size Diameter (μm)	SZ Hardness (H_v)
BM	0.89	346 ± 6.6
300/50	4.16	225 ± 4.3
400/100	6.94	221 ± 4.2
500/25	12.5	218 ± 4.2

the material, and its constitutive behavior, so that HI values from different studies cannot be directly compared. However, it does seem that FSW of ODS steels may be accomplished with lower rotational speeds and higher traverse speeds as long as the combination produces some minimum heat input to the material.

The ratio between rotational and traverse speeds, represented by the HI can be used to describe relative changes in heat input for welds made under fixed conditions (same FSW system and tool, same plunge force, same material, and material dimensions), but it is

not sufficient for predicting successful welding procedures or microstructural evolution in general. Indeed in the present work, two FSW conditions with the same HI (400 RPM/100 MMPM and 200 RPM/50 MMPM) produced successful and defective welds, respectively. So, while the HI is the same, it is clear that the heat input was not. The starting microstructure of the material clearly also plays a large role in the post-FSW microstructure. In recent research by Wang *et al.*, recrystallized, coarse grained MA956 was friction stir welded with a rotational speed of 1000 RPM and a traverse speed of 50 MMPM.^[21] The starting microstructure of this material consisted of large (200 to 500 μm diameter), anisotropic grains. After FSW, the SZ microstructure consisted of small (3.4 μm average), more uniformly shaped grains. The ratio of 1000 RPM to 50 MMPM is the same as for the 500 RPM to 25 MMPM used here. The ferrite grain size in the plate material for this study is approximately 1 μm . After FSW, the SZ ferrite grain size is 12 μm , several times larger than that reported in the recent work by Wang. This difference in SZ microstructures points out the

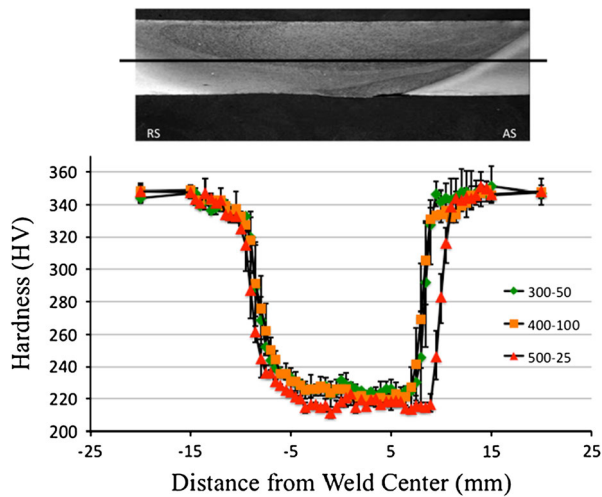


Fig. 8—Hardness profile (from left to right) across the SZ for varying FSW parameters.

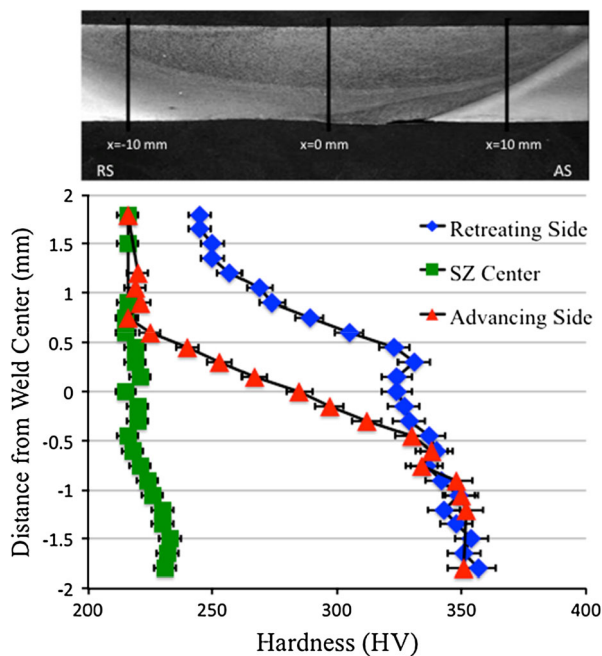


Fig. 9—Hardness profile as a function of depth (from top to bottom) along each vertical line in the weld for 500 RPM/25 MMPM weld parameters for the RS (diamonds), SZ (squares), and AS (triangles).

importance of the starting microstructure, as well as, the FSW system and tool geometry, and the heat input model for predicting the SZ grain size, even for the same nominal alloy.

More complex relationships have been used to connect microstructural evolution with heat input and FSW parameters. The homologous welding temperature (T/T_m) was observed to increase as the squared ratio of tool rotational speed to tool traverse speed (denoted as pseudo-HI by Mishra) for FSW of aluminum alloys.^[26] Other research by Wei and Nelson has included the effect of tool torque to define a heat input that is the

ratio of power (tool torque multiplied by tool rotational speed) to tool traverse speed.^[30] Comparing these metrics, Wei and Nelson concluded that heat input could be effectively described as a simple ratio of power to tool traverse speed. This combination of FSW parameters was the only metric to produce linear relationships between heat input and post-weld microstructural features such as ferrite grain size and bainite lath size in HSLA-65. Querin and Schneider have also developed an alternative HI that includes power and heat losses due to tool and anvil geometries/materials.^[33]

The stir zone microstructure observed after FSW is affected by the heat input, the intense shear deformation, and by the starting microstructure. The heat input due to FSW causes significant grain coarsening in the SZ, and the degree of grain coarsening can be directly related to the HI. FSW is a thermo-mechanical process that produces temperatures between 70 and 90 pct of the alloy melting temperature.^[26,34,35] Although we did not measure the temperature during FSW, we would estimate, based on the melting temperature of MA956 at 1755 K (1482 °C), that the temperatures might fall in the range between 1223 K and 1573 K (950 °C and 1300 °C). The continued presence of the low-angle grain boundaries (LAGBs) after FSW indicates that the grain growth is not solely a function of elevated temperatures (in which case there should be no LAGBs). Instead, continuous dynamic recrystallization is occurring as grains are both growing due to heat input and are shearing by the FSW process. In a review by Doherty *et al.*, the term “recrystallization” is defined as the formation of new grain structures in a deformed material by the formation and migration of high-angle grain boundaries driven by the stored energy of deformation, while the term “dynamic recrystallization” is defined as the occurrence of recrystallization during deformation.^[36] This dynamic recrystallization is different from the classical model of recrystallization as a seeded-nucleation and growth process. Expanding further on this theory of recrystallization, Humphreys differentiates between discontinuous processes where grain growth occurs heterogeneously throughout the material and continuous processes where grain growth occurs uniformly with no identifiable nucleation and growth stages.^[37] Based on this more descriptive definition, the term “continuous dynamic recrystallization,” as defined by Humphreys, seems most appropriate to describe FSW.

The persistent, torsional texture observed, regardless of heat input, further suggests that the SZ microstructure observed is the result of a continuous dynamic grain coarsening process during deformation. Although it has already been reported that the FSW process produces a BCC torsional texture in the SZ for other ferritic ODS steels,^[19,20] the evolved SZ texture in this research compares very closely to theoretical ideal orientations developed for texture developments during torsional deformation of ferritic steels^[38] as well as texture formation during equal angular extrusion of BCC materials.^[39] The SZ texture contains a $\langle 111 \rangle$ fiber as shown in Figure 13 and matches closely to ideal orientation points as described by Baczynski.^[38] To

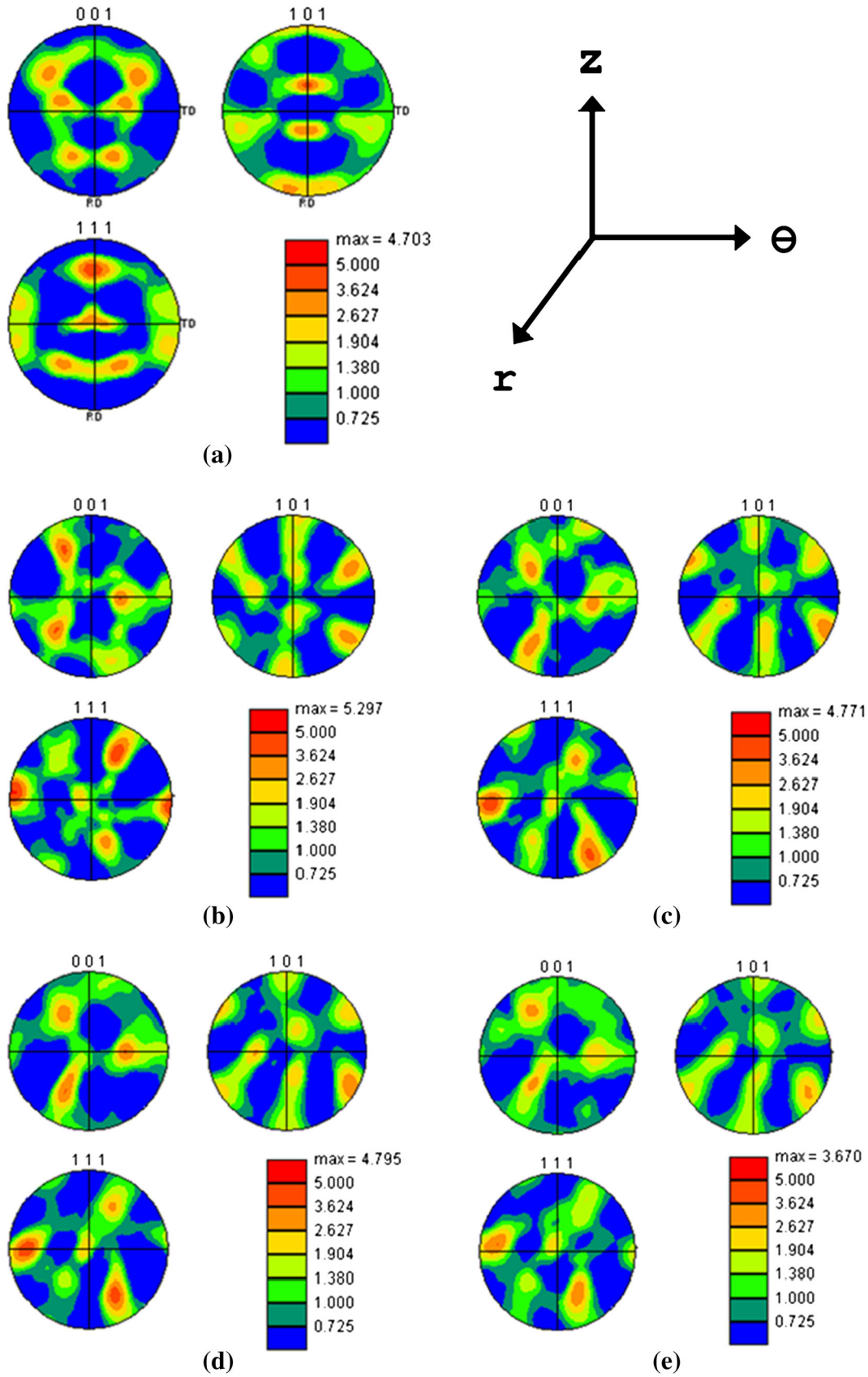


Fig. 10—Pole figures for (a) BM-rolled texture, and (b) 275 RPM/100 MMPM, (c) 300 RPM/50 MMPM, (d) 400 RPM/100 MMPM, and (e) 500 RPM/25 MMPM showing a persistent BCC torsional texture following FSW.

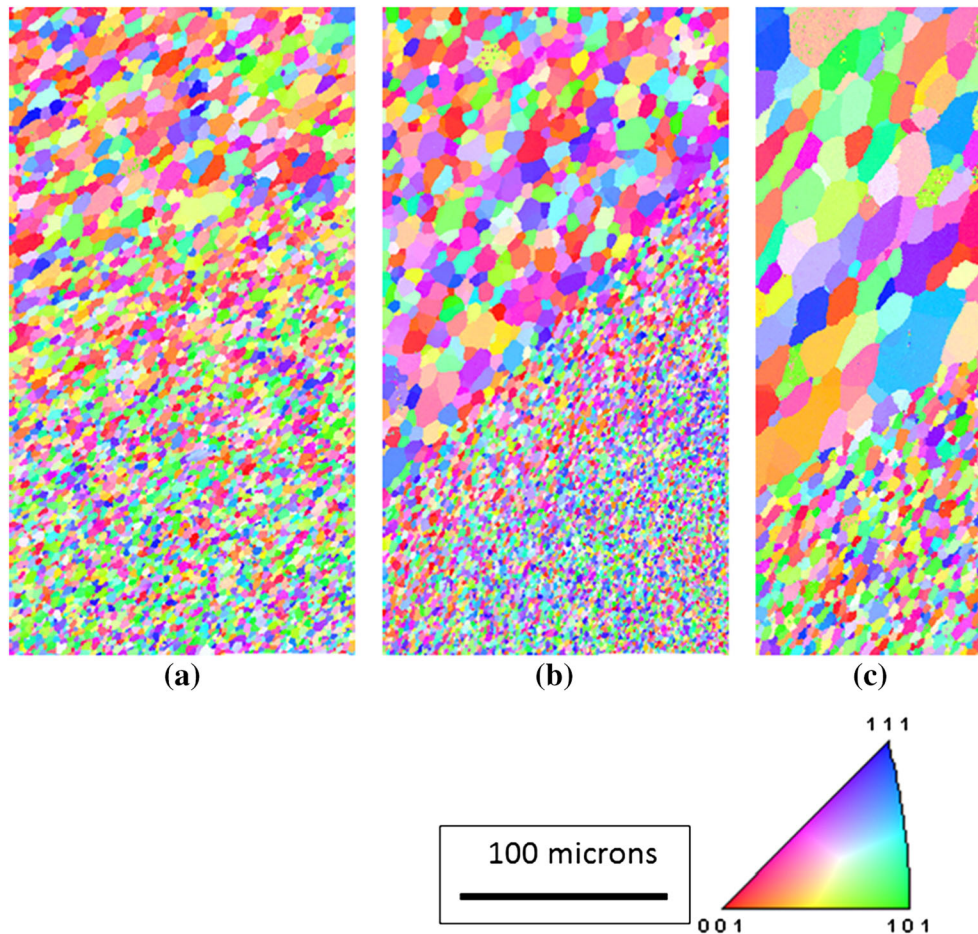


Fig. 11—SZ-TMAZ interfaces on the advancing side of the weld for (a) 400 RPM/100 MMPM, (b) 300 RPM/50 MMPM, and (c) 500 RPM/25 MMPM conditions showing the increase in microstructural gradient as a function of heat input.

allow for direct comparison to ideal shear textures, the pole figure from the SZ in Figure 13 has been rotated by the angle of the FSW tool such that the pole figure is in the actual shear plane between the tool and the work piece (as opposed to the pole figures in Figure 10 which are shown in the transverse z - Θ plane of the weld structure). This rotation results in improved alignment of peaks in the pole figures compared to the ideal texture from Baczynski. The experimental results in this work also correlate with the ideal shear texture in BCC materials identified in recent research of texture development in friction stir welds by Fonda.^[40] The torsional texture is a deformation texture that does not require recrystallization to form. No other “recrystallization” texture was observed in this work or in the literature. Thus, nucleation and growth-based recrystallization are likely not responsible for the SZ microstructure in ferritic ODS steels, which should instead be described as continuous, dynamic recrystallization.

The starting microstructure of the ODS steel is also quite important in determining the final, welded microstructure. Manufacturing techniques for MA956 ODS steels can produce plate material either in an unrecrystallized or recrystallized form. The recrystallized form is produced by a post-manufacture heat treatment that

results in a very coarse grained MA956 base material (nominally hundreds of micron grain sizes or larger).^[41–43] The distinction between unrecrystallized, fine grained MA956 and recrystallized coarse grained MA956 is significant since FSW on the two different, starting materials produces opposite results. In recent research by Wang *et al.*, recrystallized, coarse grained MA956 was friction stir welded with a high heat input (1000 RPM/50 MMPM, HI = 20).^[21] Again, this is the same HI value as that used for the 500 RPM/25 MMPM condition used in this work; however, the SZ grain size observed by Wang *et al.* is approximately 1 to 2 μm , compared with the 12 μm grain size observed in this work. In the case of the recrystallized, coarse grained MA956, the heat input from FSW causes a refinement in grain size and a corresponding increase in hardness and strength. For unrecrystallized fine grain MA956 (starting grain size of μm), FSW causes grain coarsening and a corresponding reduction in hardness and strength, see Figure 8 and work by West.^[25]

The change in grain size and hardness across the friction stir welds is asymmetric and the degree of asymmetry is a function of the heat input. The asymmetry trend in SZ hardness has been observed and commented on by several authors^[15,18,19]; however, the

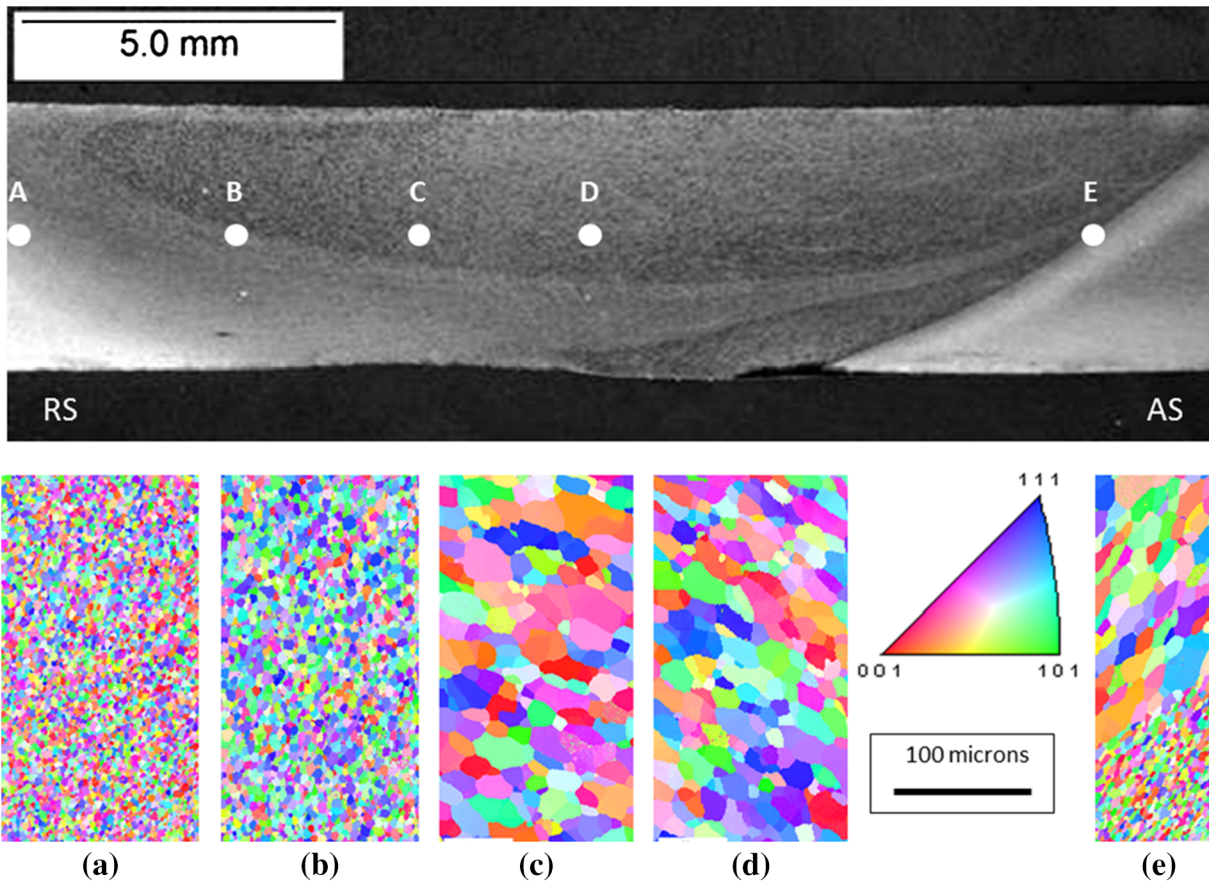


Fig. 12—Representation of IPF maps across the weld nugget for 500 RPM/25 MPM. The same 100 μm scale bar applies to all maps. Figure from Baker *et al.*^[47].

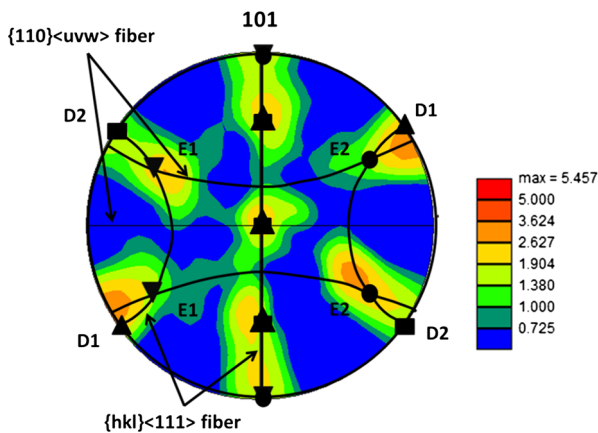


Fig. 13—SZ texture shown with overlaid ideal BCC torsional texture from Baczynski.^[38] Annotations from Baczynski: D1- $[\bar{1}\bar{1}2](111)$ (triangles), D2- $[11\bar{2}](111)$ (squares), E1- $[0\bar{1}\bar{1}](111)$ (inverted triangles), and E2- $[0\bar{1}\bar{1}](111)$ (circles). The orientation of this pole figure corresponds to the shear plane between the friction stir welding tool and the work piece. The shear direction is from left to right and the torsional axis is vertical.

analysis here also shows that the asymmetry is also a function of heat input. In addition to differences in hardness from the BM to the SZ, large gradients in microhardness exist across the weld in particular across the AS TMAZ in both horizontal and vertical directions

(Figures 8 and 9). Similar processes were conducted for other FSW conditions, and in all cases, the gradients in hardness are higher on the AS than on the RS, and the relative gradients are reduced as HI is reduced (*i.e.*, lower heat input conditions produce smaller gradients in hardness throughout the weld).

Grain size variations cross the weld, shown in Figures 4, 5, and 6, and hardness variations across the weld, shown in Figures 8 and 9, are directly related for all FSW parameter combinations. The relationship between grain size and hardness can be summarized as follows: (1) traversing from the SZ to the RS, grain size gradually decreases and hardness gradually increases, (2) traversing from the SZ to the AS, grain size and hardness are nearly constant until reaching the TMAZ at which point a very sharp decrease in grain size and increase in hardness occurs, and (3) these effects are enhanced as HI increases, *i.e.*, the SZ grain size increases for higher HI values and the abruptness of the transitions both on the RS and most noticeably on the AS is more distinct for higher HI values. The change in grain size across the weld explains the asymmetric nature of the hardness profiles and at lower HI values the asymmetry is less noticeable.

The large gradient in grain size may have significant consequence for weld reliability. The abrupt change in grain size, could lead to strain localization during tensile

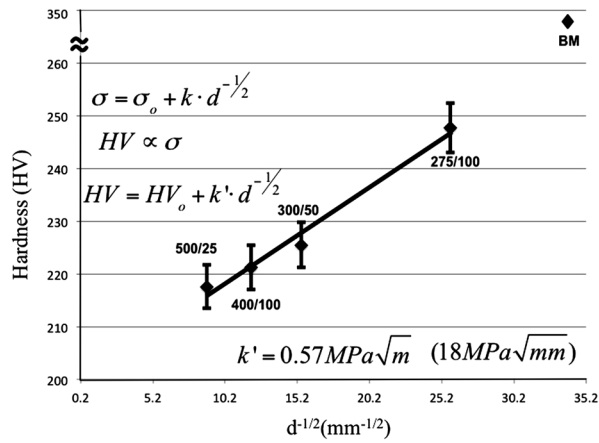


Fig. 14—Application of the Hall–Petch equation using hardness and grain size following friction stir welding. The base metal condition (BM) does not correlate with the Hall–Petch line. The y -axis is broken to show the base metal condition without vertical compression of the remaining data.

deformation across the weld. The large grain size in the SZ adjacent to the advancing side TMAZ boundary may experience a large amount of strain localization that could lead to crack nucleation at this location. FSW parameters with high heat input may need to be avoided to reduce this large grain size gradient.

The room temperature strength of the stir zone material appears to be controlled primarily by the grain size. Micro-indentation results (Figure 8 and Table III) show that FSW reduces the hardness of the BM by approximately 37 pct compared to the SZ, while the grain size increases. This grain size increase does correlate with the HI for the conditions studied in detail. The average values of hardness within each SZ show a small, but measurable, difference in hardness between the FSW conditions that may be related to the grain size. The yield strength of a material can be treated as an intrinsic material yield strength which is the sum of contributions by various strengthening mechanisms. Other authors have addressed strengthening mechanisms behind both recrystallized and unrecrystallized MA956 by summing the base material strength (σ_0) with the individual strengthening components of solid solution strengthening (σ_{SS}), grain boundary strengthening (σ_{GB}), oxide particle strengthening (σ_P), and dislocation strengthening (σ_D) (Eq. [2]).^[21,44] The conclusions from the current work and that of Wang *et al.*^[21] are that grain boundary strengthening is the dominant strengthening mechanism at room temperature in the stir zone material after FSW for both recrystallized and unrecrystallized MA956 and that this summation technique agrees with experimental results

$$\sigma_y = \sigma_0 + \sigma_{SS} + \sigma_{GB} + \sigma_P + \sigma_D. \quad [2]$$

When the current hardness data are plotted against the inverse-square-root of the grain size of the stir zone material, a relatively linear plot is observed for four of the FSW conditions (Figure 14). This linear relationship is suggestive of the Hall–Petch relationship that describes

the connection between grain size and yield strength in crystalline materials. In contrast, the hardness of the base material is much higher and does not fall on this linear regression line. It is acknowledged that hardness is a measure of a material's plastic flow resistance and is, therefore, a function of both yield strength and strain hardening. Recent work by Baker *et al.*, has performed actual uniaxial tensile experiments on material extracted from the stir zone.^[45] The room temperature yield strength of the stir zone material does, in fact, follow a Hall–Petch relationship. The major difference in the low-temperature yield strength between the base material and the stir zone material; therefore, is in the coarsening of the yttrium–aluminum–oxide particles in the material with a corresponding loss in dispersion strength. This loss of dispersion strengthening is the reason that the hardness value for the base material does not fall on the Hall–Petch line in Figure 14. More details about the evolution of these oxides and their impact on the tensile behavior of the weld material can be found in other recent work by Baker.^[46]

V. SUMMARY AND CONCLUSIONS

This paper has provided a systematic study of the processing–microstructure relationships for the FSW of MA956 ODS steel. A large range of FSW conditions were considered to intentionally vary the heat input which was simply described by a heat index, HI, the ratio of the rotational speed in RPM to the traverse speed in MPPM. Four of eight welding conditions produced defect-free full-penetration welds. Conditions that produced defect-free welds were then analyzed by OM, SEM, EBSD, and micro-indentation to determine the resulting microstructure–mechanical property relationships. The following conclusions were drawn:

1. Defect-free, consolidated welds were produced over a wide range of welding conditions with considerably lower tool rotational speeds than those previously reported in the literature. This result is important for the application of FSW to these ODS steels in terms of increased welding speed and prolonged tool life.
2. Grains in the SZ are substantially coarsened by all of the FSW conditions that created fully consolidated welds. Although the grain growth in the SZ is directly related to heat input, the persistent presence of low-angle grain boundaries and a torsional texture strongly suggest that continuous dynamic recrystallization is the operative mechanism for the microstructural evolution in the stir zone.
3. An abrupt change in grain size and hardness exists across the stir zone to thermo-mechanically affected zone boundary. This change is systematically more pronounced on the advancing side of the tool for each welding condition. Higher heat input conditions produced a more abrupt change in both grain size and hardness.
4. Hardness decreases from the BM to the SZ by up to 37 pct for each welding condition and may be corre-

lated to observed grain growth in the SZ using the Hall–Petch relationship. This result suggests that grain coarsening is the dominant, low-temperature strengthening mechanism of the welded material.

ACKNOWLEDGMENTS

This work in part was performed under the auspices of the U.S. Department of Energy by Lawrence Livermore National Laboratory under Contract DE-AC52-07NA27344.

REFERENCES

- E.E. Bloom, S.J. Zinkle, and F.W. Wiffen: *J. Nucl. Mater.*, 2004, vol. 329, pp. 12–19.
- S. Ukai, T. Nishida, T. Okuda, and T. Yoshitake: *J. Nucl. Sci. Technol.*, 1998, vol. 35, pp. 294–300.
- M.S. El-Genk and J.M. Tournier: *J. Nucl. Mater.*, 2005, vol. 340, pp. 93–112.
- I. Charit, K.L. Murty, and C.C. Koch: Advances in Materials Technology for Fossil Power Plants, *Proceedings from the Fifth International Conference*, ed. by R. Viswanathan, D. Gandy, and K. Coleman, ASM International, 2008, pp. 281–92.
- M.G. McKimpson and D. Odonnell: *JOM*, 1994, vol. 46, pp. 49–51.
- R. Lindau, M. Klimenkov, U. Jaentsch, A. Moeslang, and L. Commin: *J. Nucl. Mater.*, 2011, vol. 416, pp. 22–29.
- H.J.K. Lemmen, K.J. Sudmeijer, I.M. Richardson, and S. van der Zwaag: *J. Mater. Sci.*, 2007, vol. 42, pp. 5286–95.
- V.G. Krishnardula, N.I. Sofyan, W.F. Gale, and J.W. Fergus: *Trans. Indian Inst. Met.*, 2006, vol. 59, pp. 199–203.
- P. Miao, G.R. Odette, J. Gould, J. Bernath, R. Miller, M. Alinger, and C. Zanis: *J. Nucl. Mater.*, 2007, vol. 367, pp. 1197–1202.
- V.G. Krishnardula, R. Aluru, N.I. Sofyan, J.W. Fergus, and W.F. Gale: *Proceedings of the 7th International Conference on Trends in Welding Research*, ASM International, 2006, pp. 885–88.
- K. Shinozaki, C.Y. Kang, Y.C. Kim, M. Aritoshi, T.H. North, and Y. Nakao: *Weld. J.*, 1997, vol. 76, pp. S289–99.
- Z. Feng and W. Ren: *Proceedings of the Asme Pressure Vessels and Piping Conference 2007, vol 6, Materials and Fabrication*, 2007, pp. 431–38.
- A. Ambroziak: *Arch. Civil Mech. Eng.*, 2010, vol. 10, pp. 5–13.
- M.H. Mathon, V. Klosek, Y. de Carlan, and L. Forest: *J. Nucl. Mater.*, 2009, vol. 386, pp. 475–78.
- F. Legendre, S. Poissonnet, P. Bonnaillie, L. Boulanger, and L. Forest: *J. Nucl. Mater.*, 2009, vols. 386–88, pp. 537–39.
- C.L. Chen, G.J. Tatlock, and A.R. Jones: *J. Alloys Compd.*, 2010, vol. 504, pp. S460–66.
- A. Etienne, N.J. Cunningham, Y. Wu, and G.R. Odette: *Mater. Sci. Technol.*, 2011, vol. 27, pp. 724–28.
- S. Noh, R. Kasada, A. Kimura, S.H.C. Park, and S. Hirano: *J. Nucl. Mater.*, 2011, vol. 417, pp. 245–48.
- W. Han, S. Ukai, F. Wan, Y. Sato, B. Leng, H. Numata, N. Oono, S. Hayashi, Q. Tang, and Y. Sugino: *Mater. Trans.*, 2012, vol. 53, pp. 390–94.
- W.T. Han, F.R. Wan, B. Leng, S. Ukai, Q.X. Tang, S. Hayashi, J.C. He, and Y. Sugino: *Sci. Technol. Weld. Join.*, 2011, vol. 16, pp. 690–96.
- J. Wang, W. Yuan, R.S. Mishra, and I. Charit: *J. Nucl. Mater.*, 2013, vol. 432, pp. 274–80.
- J. Wang, W. Yuan, R.S. Mishra, and I. Charit: *J. Nucl. Mater.*, 2013, vol. 442, pp. 1–6.
- D.T. Hoelzer, K.A. Unocic, M.A. Sokolov, and Z. Feng: *J. Nucl. Mater.*, 2013, vol. 442, pp. S529–34.
- B.K. Jasthi, S.M. Howard, W.J. Arbegast, G.J. Grant, S. Koduri, and D.R. Herling: in *Friction Stir Welding Processing III*, K.V. Jata, M.W. Mahoney, R.S. Mishra, and T.J. Lienert, eds., San Francisco, CA, 2005, pp. 75–79.
- M. West, B. Jahsthi, P. Hosemann, and V. Sodesetti: in *Friction Stir Welding and Processing VI*, R.S. Mishra, M.W. Mahoney, Y.S. Sato, Y. Hovanski, and R. Verma, eds., TMS, Warrendale, PA, 2011, pp. 33–40.
- R.S. Mishra and Z.Y. Ma: *Mater. Sci. Eng. R*, 2005, vol. 50, pp. 1–78.
- B.W. Baker: Processing, Microstructure, and Material Property Relationships Following Friction Stir Welding of Oxide Dispersion Strengthened Steels, PhD Dissertation, Mechanical and Aerospace Engineering Department, Naval Postgraduate School, Monterey, CA, 2013.
- U.F. Kocks, C.N. Tome, and H.R. Wenk: *Texture and Anisotropy: Preferred Orientation in Polycrystals and their Effect on Materials Properties*, Cambridge University Press, Cambridge, 1998.
- R. Nandan, T. DebRoy, and H.K.D.H. Bhadeshia: *Prog. Mater. Sci.*, 2008, vol. 53, pp. 980–1023.
- L.Y. Wei and T.W. Nelson: *Weld. J.*, 2011, vol. 90, pp. 95S–101S.
- P. Biswas, D.A. Kumar, and N.R. Mandal: *Proc. Inst. Mech. Eng. B*, 2012, vol. 226, pp. 641–48.
- S.K. Chimbli, D.J. Medlin, and W.J. Arbegast: *Proc. 136th TMS Annual Meeting Friction Stir Welding & Processing IV Symposia*, 2007.
- J. Querin and J. Schneider: *Weld. J.*, 2012, vol. 91, pp. 76–82.
- M.W. Mahoney, C.G. Rhodes, J.G. Flintoff, R.A. Spurling, and W.H. Bingel: *Metall. Mater. Trans. A*, 1998, vol. 29A, pp. 1955–64.
- S. Swaminathan, K. Oh-Ishi, A.P. Zhilyaev, C.B. Fuller, B. London, M.W. Mahoney, and T.R. McNelley: *Metall. Mater. Trans. A*, 2010, vol. 41A, pp. 631–40.
- R.D. Doherty, D.A. Hughes, F.J. Humphreys, J.J. Jonas, D.J. Jensen, M.E. Kassner, W.E. King, T.R. McNelley, H.J. McQueen, and A.D. Rollett: *Mater. Sci. Eng. A*, 1997, vol. 238, pp. 219–74.
- F.J. Humphreys: *Acta Mater.*, 1997, vol. 45, pp. 4231–40.
- J. Baczynski and J.J. Jonas: *Acta Mater.*, 1996, vol. 44, pp. 4273–88.
- S. Li, I.J. Beyerlein, and M.A.M. Bourke: *Mater. Sci. Eng. A*, 2005, vol. 394, pp. 66–77.
- R.W. Fonda and K.E. Knipling: *Sci. Technol. Weld. Join.*, 2011, vol. 16, pp. 288–94.
- Special Metals Corporation, Engineering Data Sheet for Incoloy MA956, 2004.
- B. Dubiel, A. Czyska-Filemonowicz, and P.J. Ennis: in *Microstructural Stability of Creep Resistant Alloys for High Temperature Plant Applications*, A. Strang, J. Cawley, and G.W. Greenwood, eds., 1998, pp. 215–21.
- J.D. Whittenberger: *Metall. Trans. A*, 1981, vol. 12A, pp. 845–51.
- A.Y. Badmos and H. Bhadeshia: *Mater. Sci. Technol.*, 1998, vol. 14, pp. 1221–26.
- B.W. Baker, T.R. McNelley, and L.N. Brewer: *Mater. Sci. Eng. A*, 2014, vol. 589, pp. 217–27.
- B.W. Baker: *Mechanical and Aerospace Engineering*, Naval Postgraduate School, Monterey, CA, 2013.
- B.W. Baker, L.N. Brewer, E.S.K. Menon, T.R. McNelley, B. El-dasher, S. Torres, J.C. Farmer, M.W. Mahoney, and S. Sanderson: *Friction Stir Welding and Processing VII*, Wiley, 2013.